Engineering and Technology Journal
Journal homepage: https://etj.uotechnology.edu.iq

Tank deformation analysis by combining laser scanning and photogrammetry

Ali Salah J. Al-Saedi[a,b*], **Fanar M. Abed**[c], **Imzahim A. Alwan**[b]

[a] Surveying Department, Amara Technical Institute, Southern Technical University, Misan, Iraq.
[b] Civil Engineering Dept., University of Technology-Iraq, Alsina'a street, 10066 Baghdad, Iraq.
[c] Surveying Engineering Dept., College of Engineering, University of Baghdad, Jadriya, Baghdad, Iraq.
*Corresponding author Email: ali.alsaedi@stu.edu.iq

HIGHLIGHTS

- Integrating terrestrial laser scanning and photogrammetry enhanced data quality, comprehension, and interpretation.
- Photogrammetry is considered a complementary data source if TLS produces insufficient data.
- Measurements using fused point clouds produced reliable metric values for industrial applications.

ARTICLE INFO

Handling editor: Mohamed Mahdy Marzou

Keywords:

Terrestrial Laser Scanning (TLS)
UAV-SfM Photogrammetry
Data Fusion
Deformation Analysis
Oil Tank Calibration

ABSTRACT

Laser scanning systems are used to capture high-resolution 3D point clouds, thereby obtaining the object geometry. Terrestrial laser scanning (TLS) technology is an essential data capture tool for providing high-quality point clouds for industrial environments. However, TLS point clouds can be lacking and incomplete due to occlusions prevalent in complicated industrial environments. The static nature of the system makes it necessary to use a complementary data collection technique, such as cameras, to fill the gaps, enrich density, and improve data quality. Therefore, in this research, an integrated work frame was presented that would allow for the automatic and reliable direct co-registration of TLS data and photogrammetry of industrial objects. Combining TLS data and photogrammetric-derived SfM-MVS techniques makes getting a comprehensive dataset of complex objects possible. This is accomplished by employing individual approaches in situations that provide the most favorable conditions for operation. This research aims to detect deformation and determine the geometric features of oil plant equipment (tanks) in industrial sites. This was achieved by integrating TLS and UAV photogrammetry measurements of an oil plant in Basra City, Iraq. The gaps in the point cloud coverage introduced by TLS and UAV individual measurements are eliminated following the integration process. Detailed comparison analyses are performed on cross-sections, and the results are analyzed to show potential found to comply within a few millimeters. After data integration and accuracy analysis, the RMSE was withdrawn to reach 3 cm. This research approves the potential of data fusion to detect deformations in industrial sites.

1. Introduction

Data fusion is the process of merging data from several sensors to provide a more accurate and comprehensive 3D representation of objects compared to what can be achieved using data from a single standalone data source [1]. 3D modeling of industrial facilities, including oil plants, is necessary for several applications, such as virtual simulations, maintenance scheduling, structural studies, and safety assessments [2]. Data-collecting techniques, such as terrestrial laser scanners (TLS) and unmanned aerial systems (UAV), are employed as noncontact measurement technologies for optimal 3D point cloud reproductions. The choice of an appropriate data-integration technology depends on the object's geometric qualities, the desired level of accuracy, and the associated cost [3]. This integration combines the advantages of both technologies in one approach, allowing for the precise and comprehensive capture of delicate features and large-scale structures like never before [2,4].

In recent years, TLS has emerged as a high-precision, non-contact measurement tool in industrial applications [5]. This innovative technology utilizes laser beams to acquire 3D point cloud data of the ground objects and their surrounding environment. However, a single ground-based laser scanner cannot capture point cloud data from the top of ground objects. As a result, the 3D reconstruction models experience voids, and the rebuilt models are devoid of texture details [6]. On the other hand, UAV-based Structure-from-Motion (SfM) photogrammetry provides a supplementary viewpoint by facilitating aerial

http://doi.org/10.30684/etj.2024.153203.1810
Received 29 August 2024; Received in revised form 04 October 2024; Accepted 11 October 2024; Available online 19 November 2024
2412-0758/University of Technology-Iraq, Baghdad, Iraq

data capture over vast regions. Unmanned Aerial Vehicles (UAVs) can collect overlapping images from different perspectives rapidly and efficiently. This approach offers significant benefits in industrial environments; UAVs can easily reach inaccessible regions like the tops of tanks or any elevated structures, thereby enabling a thorough overview of the entire facility. Nevertheless, the point clouds produced by UAV photogrammetry aren't always as dense or accurate as TLS data, which might be problematic when trying to represent intricate industrial components with precise details [7]. However, none of the above techniques is limitation-free. Therefore, integrating data collected from different platforms, commonly called the "data fusion" method, must be implemented cautiously to exploit advantages and overcome weaknesses [8,9].

To demonstrate the potential of laser scanning and photogrammetric data fusion for industrial components, Lenda and Marmol [4], conducted a study to combine surveys from TLS and high-precision scanning performed by a drone (ULS) to obtain a comprehensive point cloud of a tower structure. Fusion measurements can reduce point cloud gaps and the characteristics of ULS or TLS standalone measurements. Depending on how well the ULS point cloud and TLS cloud match, the overall accuracy of the integrated data can be expected to be high. The surveys were integrated for the water tower, resulting in a coherent structure model with a mean fusion error of 13 mm. Similarly, Siwiec and Lenda [10], combined the TLS and SfM photogrammetric techniques to measure a 120 m industrial chimney. Complete point cloud coverage was needed for the model integration, with an accuracy level on par with laser scanning. The point cloud generated by the SfM photogrammetric technique was subsequently integrated into a cohesive model of the lower sections of the chimney, which was constructed using TLS. For every method, full point coverage was obtained with an external consistency of about 10 mm and an internal consistency of a few millimeters. The consistency of the TLS declined as elevation increased, causing an uneven loss of scanner range. Integrating both measurement techniques was feasible even in regions with only partial point cloud coverage. An average error of 13 mm in cloud integration was made possible by sufficient coverage that spanned approximately 55 meters. Moreover, Li et al. [11], addressed the deficiencies in image data collection by using a single drone (UAV) to capture oblique images of structures near the ground, such as bridge piers, and distinctive elements like suspension cables in bridges. Later, they used TLSs to scan the same bridge piers and found that TLS point clouds did not have any texture information, showing how hard it was to get the point cloud data for the top structures of bridges. Their study sought to create a high-precision, comprehensive, and realistic bridge model by combining TLS point cloud data and UAV image data. Their findings indicate that the geometric accuracy of the integrated data is 1.70 cm, representing a 31.5% improvement with 1.2 cm, 0.8 cm, and 0.9 cm in the X, Y, and Z directions, respectively. Further, Burdziakowski and Tysiac [12], used ship hull modeling to address the combined close-range photogrammetry and terrestrial laser scanning fields. The authors stressed precision and measurement accuracy because of their potentially complex application in ship hull inventories. The group of photogrammetry methods that rely on high-quality images is thought to be pertinent to the goal of the inventories. These techniques are combined with TLS in a novel approach. The difficulties they encountered when producing their findings are particularly notable in the case of edges; the edge registered by the laser scanner was not represented in the cloud, but photos rather represented it. Thereby concluded that it is reasonable to provide engineering measurements needing high accuracy (less than 1 cm) when combining photogrammetry and laser scanning data. In addition, the study by Guo et al. [13], utilized multisource remote sensing for air-space-land integration to monitor the external liquefied natural gas (LNG) tanks. This task is crucial for ensuring national energy security since LNG storage tanks are a vital infrastructure. They incorporate control measurements, LiDAR, UAV photogrammetry, thermal infrared camera monitoring, interferometric synthetic aperture radar (InSAR), and other techniques. The data analysis revealed a few issues, including monitoring a single research object using a single technique, which results in incomplete and insufficient monitoring data. With an emphasis on the abovementioned topics, they created a program for monitoring the integrity of LNG external tanks by combining thermal infrared detection, UAV photogrammetry, ground-based and unmanned aerial LiDAR, and InSAR settlement techniques. This allowed us to monitor the integrity of LNG external tanks through multi-technology fusion and air-space-land integration. Lastly, Soni et al., [14]. Explore various methodologies for structural monitoring in the rail industry, particularly focusing on TLS and CRP. It highlights the limitations of traditional monitoring methods, which often require intrusive setups involving fixed targets like prisms, making them costly and complex in railway environments. Generally, integrating these advanced techniques presents a significant advancement in structural monitoring within the rail industry. The paper also references the need to understand data quality and structural characteristics to validate the observed changes.

The objective of this research is to combine two standalone Remote Sensing (RS) techniques, namely TLS and UAV photogrammetry, to create an integrated model that provides complete point cloud coverage while maintaining an accuracy that outperforms standalone techniques for deformation monitoring of industrial objects. As a result, ground-based laser scanning was utilized to produce a coherent point cloud model of the lower parts of an oil tank industrial facility. This model was then co-registered to the point cloud generated by the SfM-MVS photogrammetry approach. Appropriate constraint points were selected to integrate the clouds, and the accuracy of the entire model was validated by analyzing the coherence of the selected cross-sections obtained from individual methods. These sections were selected at locations without common observation coverage to check validity.

2. Materials and methods

Several geomatic approaches are applied to accomplish the study goal and fulfill research objectives. Innovative digital techniques are utilized after considering the characteristics of the tanks in the oil plant and the availability of digital sensors. Considering the available platform sensors, a data fusion methodology was broken down into three essential steps. The data

from TLS and UAV were processed individually before being combined in a co-registration workflow. Figure 1 depicts the synoptic workflow of the presented study, which will be explained in detail in the following sections.

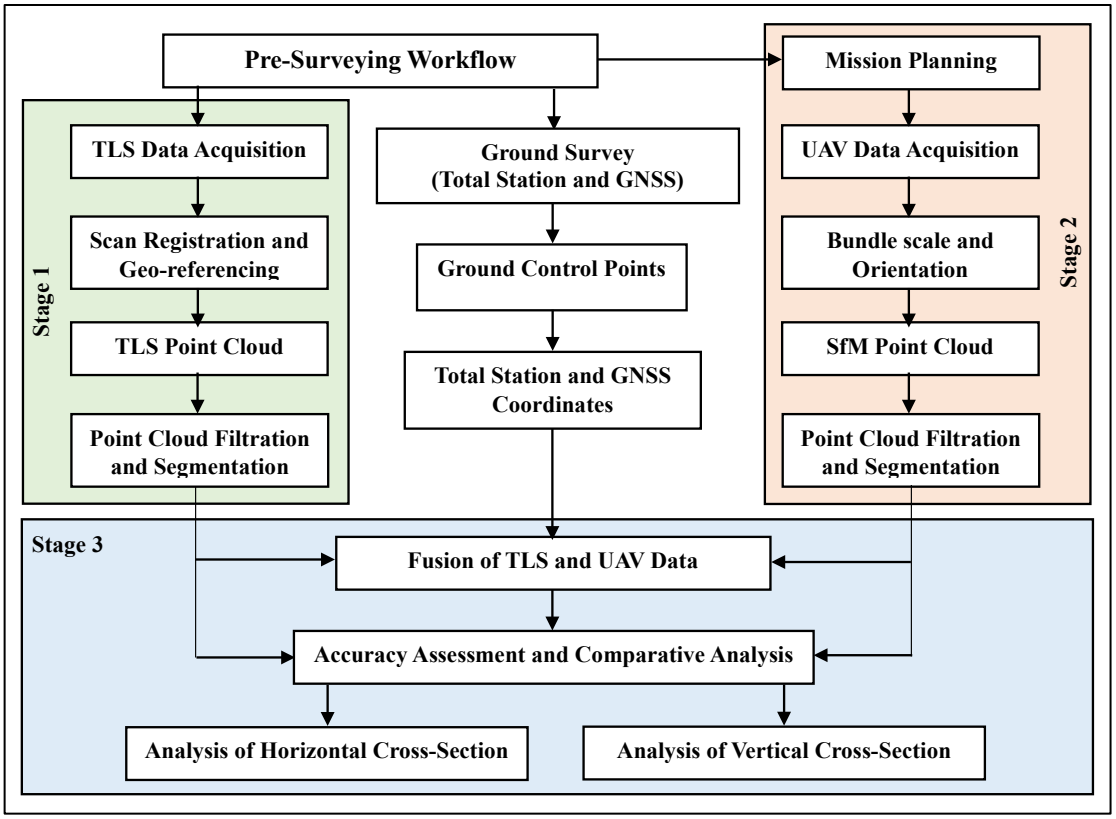

Figure 1: Synoptic study workflow

2.1 Study area – The object of interest

A part of an oil plant facility, specifically the oil tanks, is selected to be the Object of Interest (OOI) in this study. This part of the facility was chosen because it should enable the observation of problems associated with terrestrial laser scanning while also providing the capability to acquire point clouds using both techniques over the greatest length. The structures of the tanks were made of reinforced concrete, and they stood at a height of 8 m and a diameter of around 13 m Figure 2a. It was erected using the climbing formwork method, not with excessive precision, which left characteristic marks. The study area, located in Basra Governorate, southern Iraq, and the OOI was chosen for its complexity and intricate details that demand high accuracy in the modeling process. This underscores the need for high-precision monitoring techniques. Furthermore, the study area provides ample space to conduct various geomatic surveys, ensuring the best possible workflow for accurate comparison and evaluation.

2.2 Field surveying and point cloud generation

Several geomatic techniques are used for collecting data needed to create accurate 3D models, such as photogrammetry, laser scanning, and other traditional survey instruments like total stations and GPS/GNSS devices. TLS and RTK UAV were the primary data acquisition technologies utilized. Total Station Leica TS09 Plus and CHCNAV i50 GNSS receiver were utilized to georeferenced the collected data to the state coordinate system and measure TLS control points and photogrammetry checkpoints, (see Table 1).

Because fusion is a hybrid approach that links data that is referred to the same reference system, it was necessary to construct a reference network that would integrate the two techniques into the World Geodetic Reference System 1984 (WGS84). As a result, two reference networks were formed using GNSS and TS measurements. GNSS provides accurate positioning for the main closed traverse points, supports UAV image processing, and serves as a baseline for total station measurements to precisely observe target points on the object of interest (OOI), see Figure 2a, which are subsequently used in registering TLS scans following the Iterative Closest Point algorithm (ICP) [15]. However, GNSS measurements were used to integrate the two combined datasets into one World Geodetic Reference System following geo-referencing for validation.

The SfM photogrammetric technique was applied in a standalone process to align the projection centers of the aerial photographs and process dense 3D point clouds. Artificial checkpoints were measured in the field and examined in the photogrammetric program to provide a high accuracy rating. The same methodology was used to measure the TLS targets and these checkpoints in individual workflow. The checkerboard targets temporarily stabilized these points, which were made of square paper (210 mm × 210 mm) in dimensions and were measured without a prism, as shown in Figure 2b. The targets were positioned in high- and low-level positions and distributed in a regular geometric distribution. The total number of

checkerboard targets (GCPs) was 34, those subjected to raw measurement errors. 24 GCPs were used as a control reference, whereas 10 GCPs were used as checkpoints. The GCPs coordinates were determined in site with a less than one-millimeter standard deviation, Figure 2c.

Table 1: Technical specifications of the devices used

No.	Device	Characteristics		
a		**Leica TS09 Plus [16]**		
		Angle Measurement	Accuracy	1" (0.3 mgon) / 2" (0.6 mgon)
			Method	Absolute, continuous, diametrical: at all models
		Distance Measurement	Accuracy (with Reflector)	Precise+: 1.5 mm + 2.0 ppm Precise Fast: 2.0 mm + 2.0 pp
			Accuracy (without Reflector)	2 mm + 2 ppm
b		**CHCNAV i50 GNSS [17]**		
		Characteristics	Channels	432
			GPS / GLONASS	L1, L2, L5 / L1, L2
			Galileo / BeiDou	E1, E5a, E5b / B1, B2, B3
			Real-Time Kinematics (RTK)	H: 10 mm + 1 ppm RMS V: 15 mm + 1 ppm RMS
			Post-Processing Kinematics (PPK)	H: 3 mm + 1 ppm RMS V: 5 mm + 1 ppm RMS
			Post-Processing Static	H: 3 mm + 0.5 ppm RMS V: 5 mm + 0.5 ppm RMS
c		**Leica ScanStation C40 [18]**		
		Main Characteristics	Type	Ultra-high-speed time-of-flight laser scanner
			Field of view	Horizontal —360° Vertical —290° (max.)
			Scan rate	up to 1,000,000 points per second
			Range and reflectivity	Minimum 0.4 m, 270m at 34%; 180m at 18%
		Accuracy	Distance measurement	1.2 mm
			Angular measurement	8″ horizontal; 8″ vertical
			3D position	3 mm at 50 m; 6mm at 100 m
			Target acquisition	2 mm standard dev. at 50 m
d		**UAV DJI Phantom 4 Pro [19]**		
		Aircraft	Weight	1380 g
			Max. flight time	28 min.
			Max Flight Speed	20 m/s
			Max Ascent/Descent Speed	6 m/s/4 m/s
			Satellite positioning system	GPS/GLONASS
		Camera	Operating Environment Temperature	0–40 °C
			Sensor	1″ CMOS
			Image size	4864 pixels × 3648 pixels (4:3)
			Effective Pixels	20 Megapixels
			Gimbal pitch	- 90 to +30°

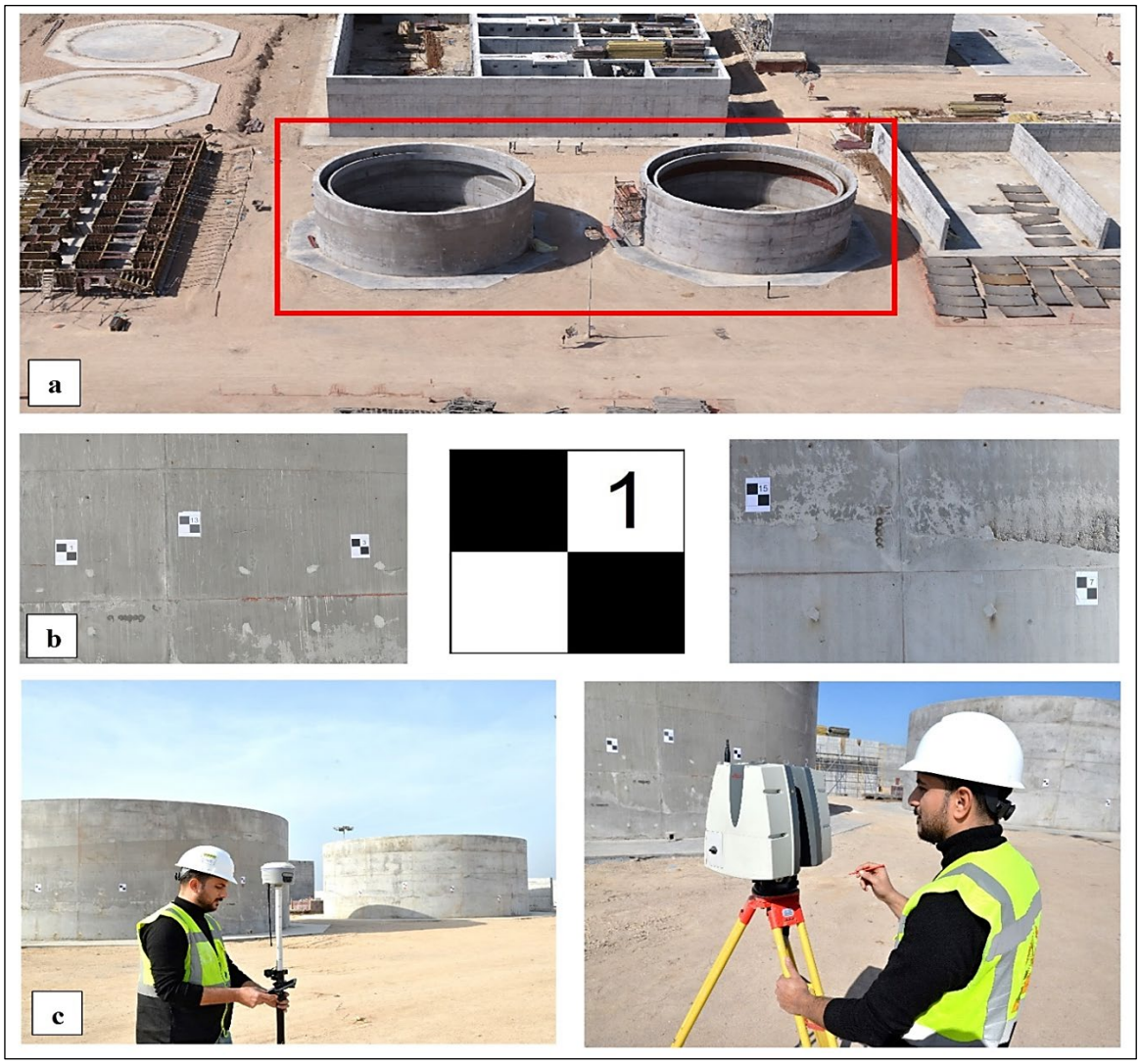

Figure 2: Target distribution and data collection: (a) Case study showing OOI, (b) Checkerboard targets and distribution , (c) Data acquisition

2.2.1 UAV Data acquisition

The DJI Phantom 4 Pro unmanned aerial vehicle was utilized for aerial imaging. The research was carried out to construct a complete 3D object model. It used the data collected from the UAV method to fill the gaps available in the roof data of the tanks collected using the TLS method. The GNSS device and UTM projection system were used to obtain the coordinates of the five Ground Control Points (GCP) created around the building before the unmanned aerial vehicle (UAV) flight. A flight plan that included high-resolution images and quality block geometry had to be established to guarantee the standards were met. This was necessary since the photogrammetric data must be combined with the laser data during the post-processing stage. Using the PIX4DCapture [20,21], a flight plan was developed to acquire aerial images of the OOI roof using UAV photogrammetry. A low flight with a vertical (nadir direction) setting was applied. Later, another coverage was operated with an oblique setting (45° angle concerning the horizontal level) to deliver a dense coverage from multiple Fields of View (FOV). Optimal overlap settings are configured, and crossed patterns are operated to ensure high image matching points. This decision was made based on optimal flight plan considerations to obtain a high level of detail that was present at the industrial site. The GSD value was calculated as demonstrated in Equation 1 [22]. The flight was planned using the dual grid method following computed flight parameters to collect the photographic data as illustrated in Equations (2-9) [22].

$$GSD\ (m/pix) = \frac{flight\ altitude \times sensor\ size}{focal\ length \times image\ size} \quad (1)$$

$$End\ lap\ \ (PE) = \left(\frac{G - B}{G}\right) \times 100 \quad (2)$$

$$Side\ lap\ \ (PS) = \left(\frac{G - W}{G}\right) \times 100 \quad (3)$$

$$Distance\ between\ flight\ lines\ (SP) = (w) \times \left(\frac{100 - PS}{100}\right) \quad (4)$$

$$Number\ of\ flight\ lines\ (NFL) = \left(\frac{Width}{SP}\right) + 1 \quad (5)$$

$$Distance\ between\ two\ consecutive\ images\ (B) = (l) \times \left(\frac{100 - PE}{100}\right) \quad (6)$$

$$Number\ of\ images\ (NIM) = \left(\frac{Length}{B}\right) + 1 \quad (7)$$

$$Total\ number\ of\ images = NFL \times NIM \quad (8)$$

$$UAV\ speed\ (m/s) = \frac{GSD \times maximum\ motion\ blur}{Shutter\ speed} \quad (9)$$

where G is the dimension of the ground that a single vertical photograph covers, B is the distance between stereo pair exposure stations, w is the spacing between flight lines, and w and l represent image ground coverage width and length, respectively. Following the execution of the flight plan, 426 images were collected, with a Ground Sampling Distance (GSD) of 1.51 cm/pix, 80% and 70% side forward and side lap overlap, respectively. The flying height was approximately 25 m, and the flight speed was 15 m/s. Figure 3 depicts the aligned images, the dense point clouds obtained, and the error estimation outcomes following the bundle adjustment workflow. The ground coordinates of the 3D point clouds are later computed through Structure from Motion Multi-View Stereo (SfM-MVS) algorithms and following the bundle block adjustment approach illustrated through the Epipolar geometry concept and collinearity equations as illustrated in Equation 10 [15,23]:

$$x = -f\frac{[m_1(X-X_S)+m_1(Y-Y_S)+m_1(Z-Z_S)]}{[m_3(X-X_S)+m_3(Y-Y_S)+m_3(Z-Z_S)]} \quad (10)$$

$$y = -f\frac{[m_2(X-X_S)+m_2(Y-Y_S)+m_2(Z-Z_S)]}{[m_3(X-X_S)+m_3(Y-Y_S)+m_3(Z-Z_S)]}$$

where (x, y) represents image point coordinates, f represents focal length, X, Y, Z represents object point coordinates, X_S, Y_S, Z_S represents the coordinates of the exposure station S in the object space system, and m is the element of the rotation matrix [24].

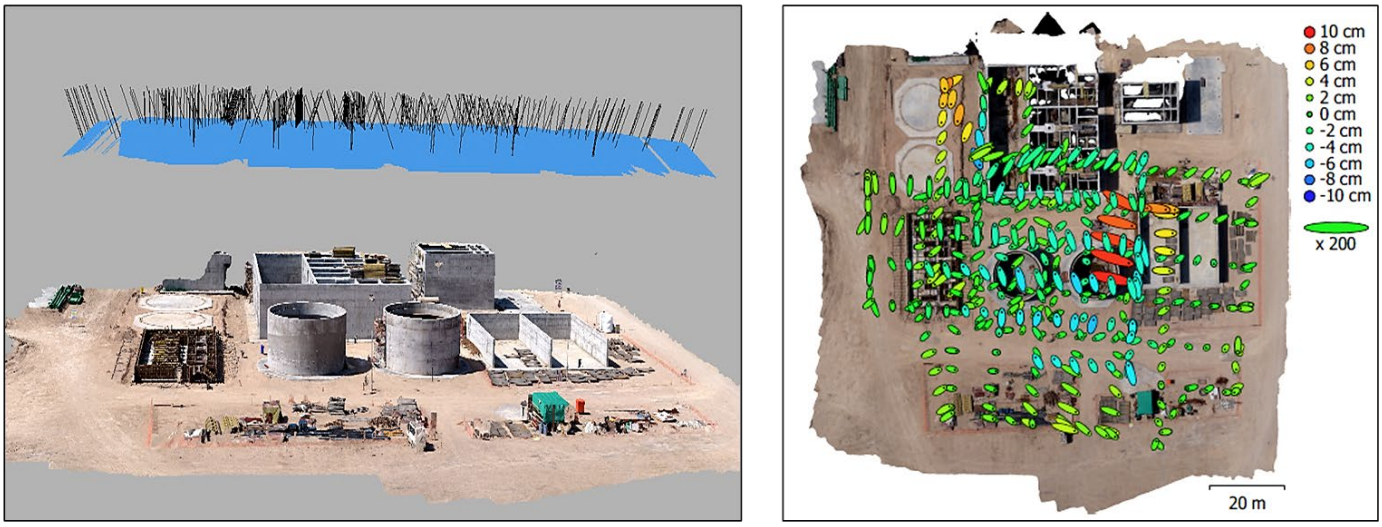

Figure 3: UAV photogrammetry process; (a) Dense 3D point clouds, (b) Camera locations and error estimates

2.2.2 TLS Data acquisition

The Leica Scan Station C40 was the TLS device for laser data collection. A geodetic tripod was used to hold the instrument while it was being measured. To achieve sufficient overlap and good visibility with the checkerboard targets, laser scans were set to collect data at close range 10 m while base distances between stations ranged from 5 to 9 m. The checkerboard targets were set earlier on the OOI and utilized as reference ground truth targets (GCPs) for TLS surveying. The camera included in the TLS was used to take panoramic photographs at the end of each scan. These images were used to determine the color of the points in the cloud following the image normalization process. The Leica Cyclone 2022 [25], was used to register scans following the coarse-to-fine process using the ICP algorithm. The RMSE of the registration of all 30 scans has a 2 to 4 mm registration error following the global-wise registration approach. The checkerboard targets were utilized to carry out the point cloud georeferencing and facilitate the registration process. Figure 4a depicts the raw point cloud produced, which included 97 million points. After filtration and removing outlier points, the resulting point clouds comprised 55 million points refer to Figure 4b. Referring to Equation (11), the time-of-flight (TOF) pulse ranging method applies to determine the laser beam's horizontal and vertical angles (β & α) and calculates the distance (D) between every 3D point and the laser instrument. Thus, the scanned target point P coordinates are computed [11]:

$$X_P = D \cos\beta \cos\alpha$$
$$Y_P = D \cos\beta \sin\alpha \quad (11)$$
$$Z_P = D \sin\beta$$

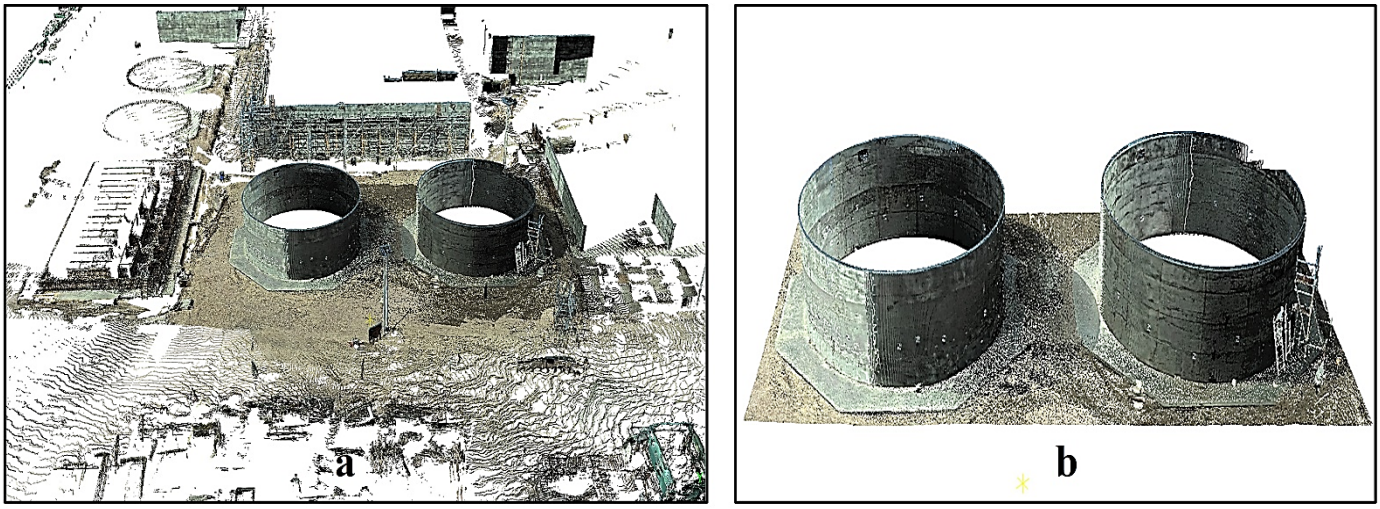

Figure 4: TLS point clouds; (a) Raw data; (b) Point clouds following filtering and outlier removal

2.2.3 Data fusion

Integrating digital photos with laser scans can surpass individual methods' drawbacks and produce better results in various settings. As a result, a flexible fusion strategy that guarantees precision, dependability, and consistency is required. Finding a co-registration technique that combines the benefits of TLS and photogrammetry, their great efficiency and minimal human intervention is the main issue in fusing laser scans with digital images. In general, co-registration can be applied manually or automatically by choosing a target group that matches the scene. Although human registration requires a lot of time and is prone to mistakes, automatic registration is a valuable technique. Therefore, an automatic co-registration approach was applied and validated in this research. Typically, automatic co-registration techniques extract unique matching characteristics to register heterogeneous datasets, such as digital images and laser scans. However, automatic feature extraction from 3D point clouds remains computationally demanding and intricate. Thus, reducing the complexity of the 3D feature extraction to a 2D problem is a flexible approach in laser scanning technologies. This solution converts the 3D laser scans into RGB and reflectance images [26]. Eventually, a single structure-from-motion procedure will be able to automatically register both these artificial laser images and camera images by using Equation 12.

$$\sum_{i=1}^{N} \sum_{j=1}^{M} \left\| x_{ij} - K_j \left(R_j X_i + T_j \right) \right\|^2 \quad (12)$$

where N is the number of 3D points, M is the number of images, x_{ij} represent the observed 2D point in image j corresponding to the 3D point X_i, R_j rotation matrix and T_j is the translation matrix.

3. Results and discussion

3.1 UAV Data processing

The Agisoft Metashape® software version 1.7.4 [27], carried out the processing steps of UAV-SfM, including camera calibration. A total of 12 GCPs were utilized to ascertain the quality of the scale of the model extracted and the georeferencing, with an overall RMSE value of 11 mm. The processing options included a "High" parameter for alignment, which means a full resolution of the images is used, and reconstruction without depth filtering, which stated the quality as "high." The raw, dense point clouds had an average ground sample distance value (GSD) of 1.51 cm/pix. They contained roughly 75 million points, see Figure 5. After removing unnecessary points, the final point clouds are estimated to comprise around 20 million points. A realistic 3D model was extracted using considerable point cloud data. Processing results from the Metashape environment can produce various products, such as mesh, orthomosaics, digital elevation models, and sparse and dense point clouds, as illustrated in Figure 5.

Figure 5: Output products of SfM photogrammetric workflow: (a) Spare cloud, (b) Dense cloud, (c) Mesh, (d) UAV 3D Model, (e) DEM, (f) Orthomosic

3.2 TLS Data processing

Initially, after completing the data collection using the laser device Leica ScanStation C40, the Leica Cyclone 2022 [25], preprocessed the data and converted all the raw files into a 3D point set format. The point clouds laser scans are then registered following the ICP cloud-to-cloud method, using the paper target markers placed homogeneously on the tank facades. At least six targets were utilized to register individual scans with their neighboring corresponding scans. Additionally, a constraint was implied in pair-wise and global-wise registration processing to ensure high-accuracy results. The pair-wise registration error was a maximum of 5 millimeters, while the global-wise registration error was 3 mm. The registered dataset was then exported for post-processing following the georeferencing process. The point clouds are later cleaned of unnecessary information and noise by removing points outside the OOI (tank shell and structural elements). This was applied using SOR and Noise filters provided in the Cloud Compare (CC) environment. Later, meshing and modeling proceeds to extract the solid surface of the OOI m (see Figure 6). Also, Figure 6 represents the geometric dense point clouds, dense clouds showing intensity values, and the final 3D solid surface model. Evidently, the necessary point density was not obtained at high points, such as ceilings or upper parts of the walls.

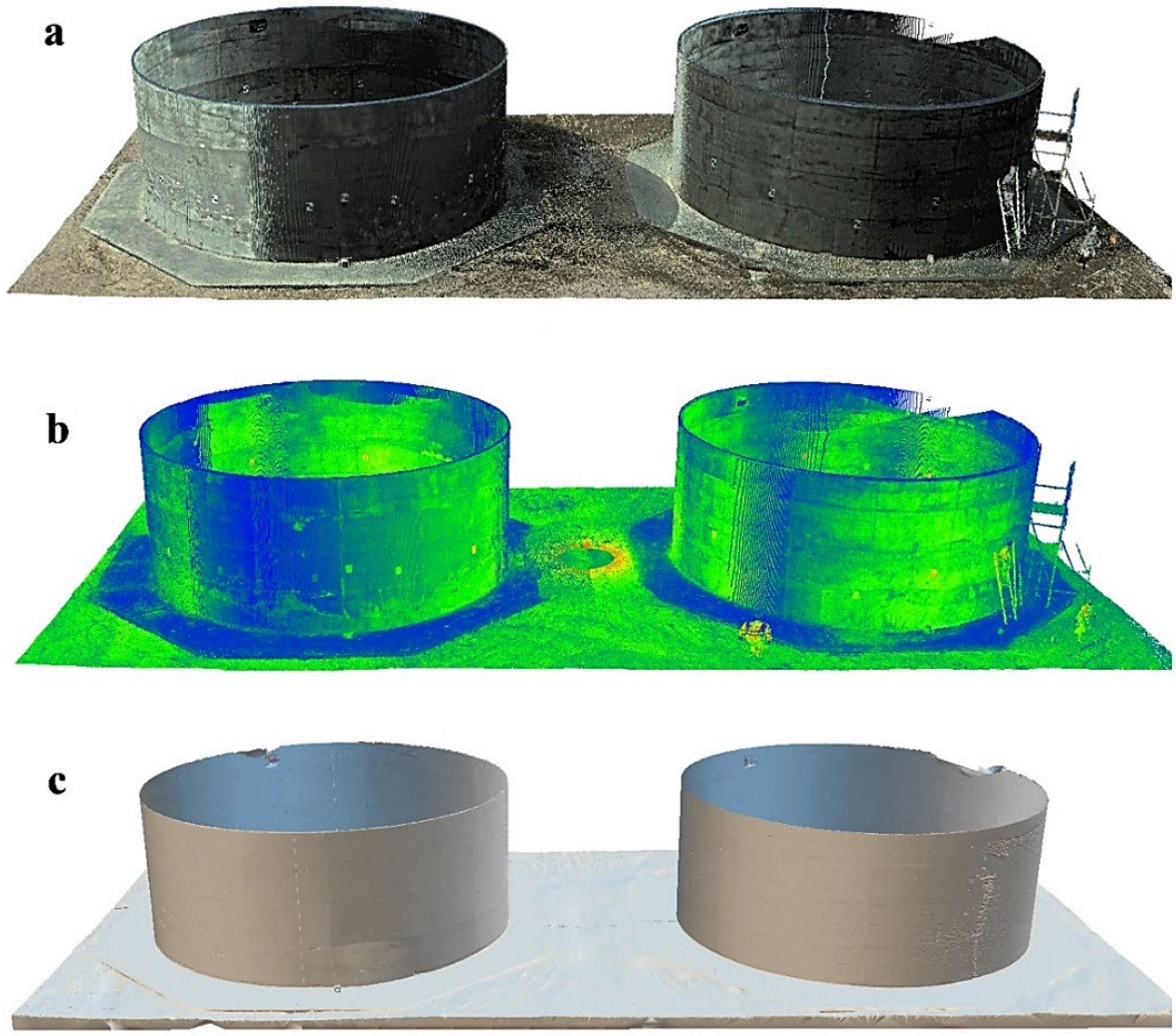

Figure 6: Output products of TLS workflow: (a) Dense point cloud, (b) Point clouds showing intensity values, (c) TLS 3D Model

3.3 Fusion TLS and photogrammetry

The TLS data was automatically combined with photogrammetric data in one standalone approach following the reality capture workflow. This was applied by converting the 3D laser data into 2D RGB images based on the e57 file format to obtain synthetic images from laser data. Later, these synthetic images are combined (fused) with the photogrammetric 2D images in the fully automatic workflow. Reality Capture (RC) can co-register TLS and photogrammetric datasets in one work frame, with three levels of detail (LOD) preview, standard, and high [28]. Reality Capture software combines the densification and meshing processes into a single procedure. While building meshes on the highest LOD is ideal, it may result in large (high-poly) models that are too complex for standard computers. To minimize the number of mesh polygons to a manageable amount, RC provides configurable mesh-simplification techniques [28]. RC uses "simultaneous bundles block modifications" of laser scan and camera photographs to fill in gaps and improve the texture of the OOI. "Simultaneous bundles block modifications" of laser scan and UAV camera photographs are utilized by RC software, which contrasts other approaches. By combining the two datasets with GCPS in one SfM paradigm, we can achieve accurate image orientation and sparse point clouds in the WGS 84 coordinate system. Registration, meshing, texturing, and coloring are features included in the fusion data scenario generated by the RC software from two datasets. Generally, high buildings present common challenges in TLS as the details at the top are unreachable (occluded) from ground acquisition stations. Such issues have been effectively resolved by fusing laser scans with images acquired by drone camera coverage. Figure 7 illustrates the completed photorealistic result of the fusion approach applied to the oil tank. However, Figure 8 represents a close view of the solid surface of the tank facades, demonstrating the deformation in this surface.

Figure 7: Fused 3D model of the tank using a co-registration approach

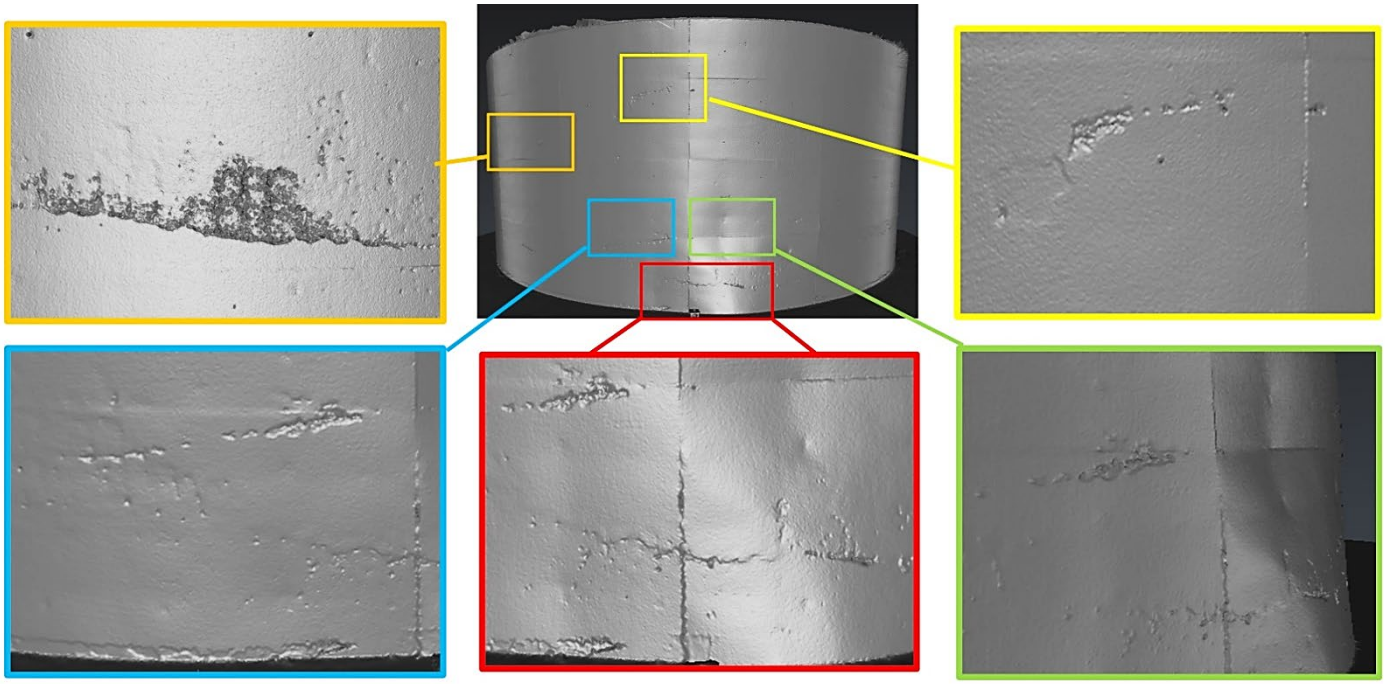

Figure 8: Tank deformations detection from fusing laser scans with dense UAV images

3.4 Comparative analysis

This research involved much visual and statistical analysis to validate the co-registered model outputs developed using the fusion approach. It was necessary to conduct a quality control accuracy assessment to check the validity of the outcomes. To get the best results possible, it was determined to conduct the validation approach based on the reference control points collected using conventional procedures once the adjustment process was finished. It was also necessary to investigate occlusions of TLS data to detect data gaps and poorly captured and noisy regions of TLS coverage, which can be discovered. Photogrammetry is used to overcome these shortcomings in an improved process, which is then applied through fusion workflow. The application's advanced analysis filters can detect various difficulties, such as roughness, 3D inspection, and cross-section analysis. So, statistical and visual analysis are applied to compare and verify the validity and ensure data quality before and after data fusion.

3.4.1 Roughness analysis

Most Time of Flight (TOF) scanners are subject to noise (or roughness) during data collection, mainly affecting range computations. It is possible to assess the roughness of point clouds by determining the distance between each point and the best-fitting plane computed based on the points' closest neighbors. In this respect, the Cloud Compare software [29], provides a broad set of tools, with roughness calculated by defining the radius of a sphere centered on particular points [30]. For example, Figure 9 contains the color map of the three datasets that explain the roughness of the 3D point clouds and their distribution with scale color, showing the relation between these points. Hence, the roughness of the UAV-imagery point cloud mean was (0.00151), and the standard deviation was (0.00141) when compared to the roughness of a TLS point cloud mean (0.00125) and standard deviation (0.00105). However, integrating laser scans and digital images in the fusion scenario has significantly reduced the roughness level of UAV-image data, where the mean became (0.00129) and its standard deviation was (0.00111).

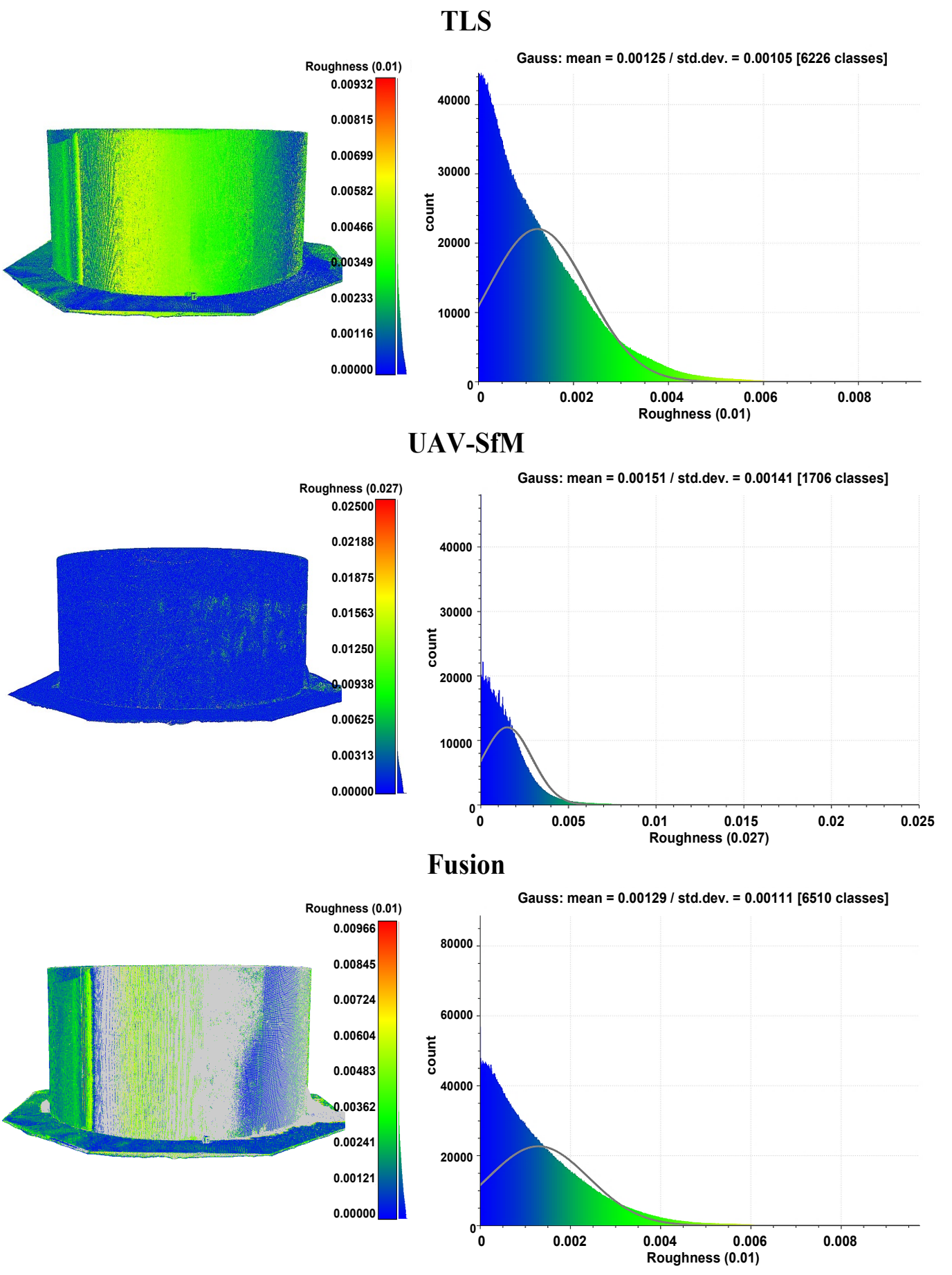

Figure 9: Roughness color maps of the tank, (a) TLS, (b) UAV-SfM, (c) Fusion

3.4.2 3D Inspection analysis

This computes the deviations from the tank's shell compared to the best cylinder. The deviations are displayed and analyzed in Figure 10. This Figure illustrates the degree of variation between the fitted least squares model and the actual model of points driven by TLS and photogrammetry approaches. The difference was represented by using different color gradients using Cyclone 3DR software, which provides a detailed analysis that helps assess the structural integrity of cylindrical objects like tanks and ensures compliance with standards such as the American Petroleum Institute (API) 653 [31]. Use Cyclone 3DR to fit a cylinder to the point cloud data representing the actual cylinder. For each point $P = (P_x, P_y, P_z)$ in the point cloud, calculate the deviation from the fitted cylinder. The deviation d_i, for each point calculated using the equation below:

$$d_i = \delta_i - r \tag{13}$$

where δ_i is calculated as:

$$\delta_i = \|q_i - c_i\| \tag{14}$$

Here, δ_i is the radial distance of the point from the cylinder's axis, c_i is the closest point on the cylinder's axis to q_i, and r is the radius of the best-fit cylinder. Figure 10 shows that using the photogrammetric technique, the highest average deviation was computed to be 0.134 m, and the lowest amount was computed to be 0.003 m. On the other hand, using the laser scanning technique, the highest and lowest average deviations were 0.124 m and 0.006 m, respectively.

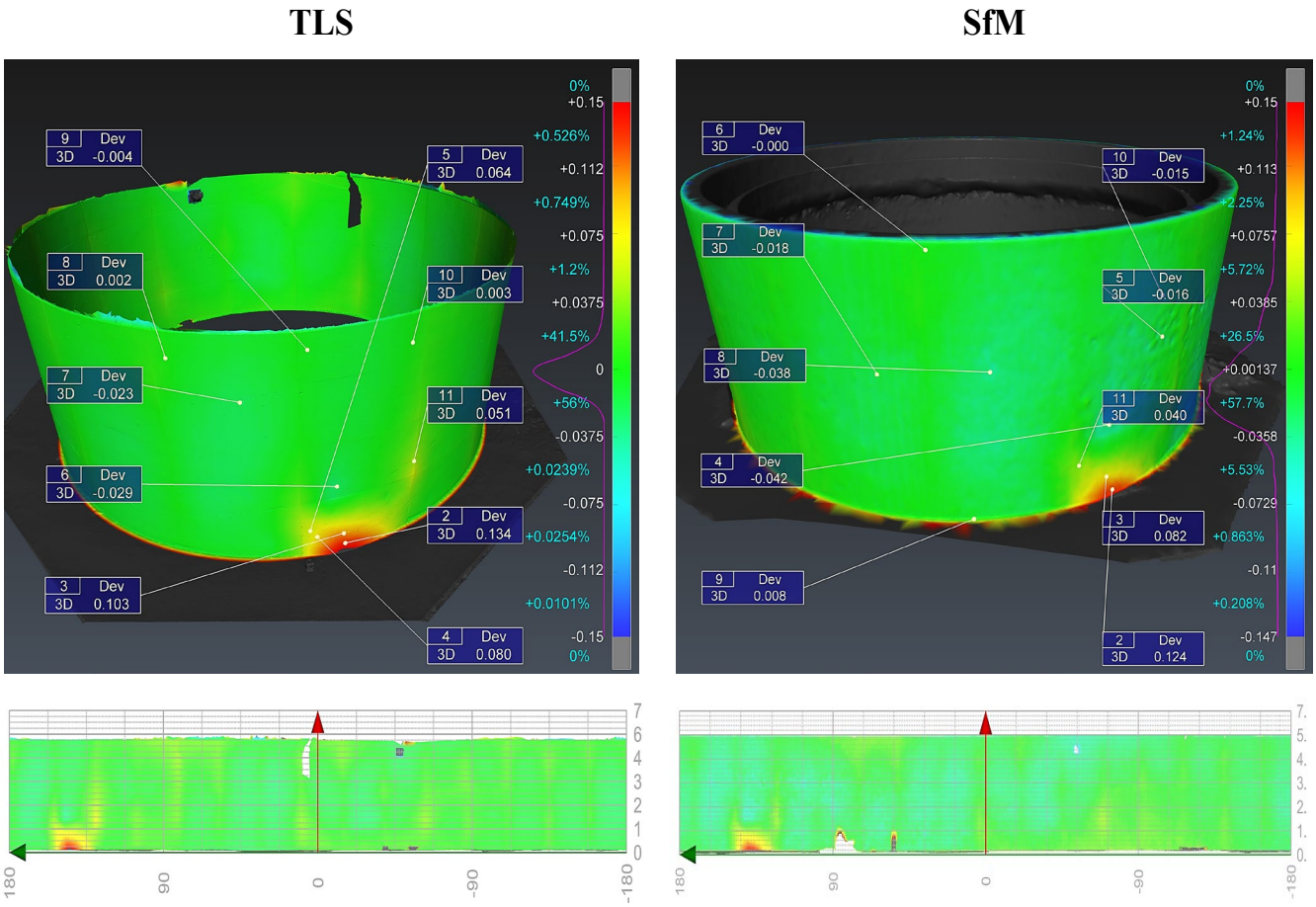

Figure 10: Color map of average deviation in standalone techniques

3.4.3 Cross-section analysis

As previously discussed, the tank's shell can be fully inspected in 3D. Additionally, it can be examined using horizontal or vertical cross-sections to assess the tank's roundness and verticality. Horizontal cross-sections were evenly distributed along the tank using Leica Cyclone 3DR software [31]. To adequately cover the typical cloud range, 14 cross-sections were designed, positioned vertically at intervals of 0.5 m. However, full coverage was achieved only at the ten lowest cross-sections due to significantly reduced scanner coverage at certain sites. Furthermore, two vertical cross-sections, oriented perpendicularly to each other, were selected for analysis. Figure 11 illustrates the configuration of the cross-sections obtained from both horizontal and vertical directions.

Due to the study's limited scope, graphical analyses were restricted to the first four horizontal cross-sections, as shown in Figure 15. In contrast, numerical results of the comparisons, presented in Table 2 and Figures 12–14, were applied to all horizontal cross-sections. Similarly, the vertical cross-sections are detailed in Table 3 and Figure 16.

Cloud segments with a height of 5 cm were selected to generate the cross-sections. These segments were projected onto a plane to ensure that the circle fitting and deviations were determined in the horizontal plane. Subsequently, the least squares method was employed to fit a circle to the dense cloud. In addition to graphical assessments, numerical parameters were calculated for each cross-section, enabling further evaluation of the fusion dataset accuracy.

Two parameters were used to assess internal consistency. The first was the deviation of the TLS and SfM clouds from the fitted circles, and the second was the variation in circle radius values between TLS and SfM data. External consistency was evaluated using three parameters [2,4,10]. These included the integrated cloud's deviation from the fitted circle (Figure 12), as well as the differences in circle radii and center coordinates between TLS, UAV-SfM, and the integrated cloud (Figures 13 and 14). The summarized results are provided in Table 2.

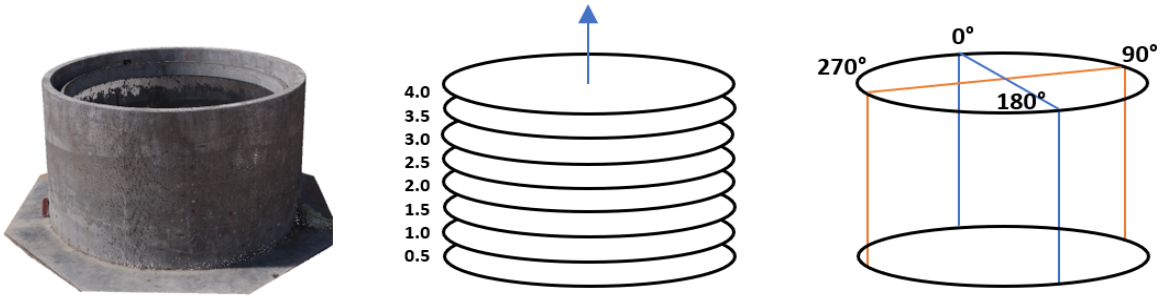

Figure 11: Horizontal and vertical cross-sections

The graphic analysis revealed a significant similarity between the cross-sections' outcomes. Compared to the fitted circles, the deviations occurred in the same locations and mostly had the same values within the intervals set every 10 mm. It was found that the results of the fusion, TLS, and photogrammetry were different. Compared to terrestrial scanning, the photogrammetric data density on the tank support's lowest cross-sections was significantly lower, and the data scatter was significantly high. The average deviations for TLS range between 3.1 mm and 4.9 mm, showing a relatively consistent performance across sections. UAV-SfM, however, presents higher deviations, between 4.4 mm and 5.5 mm. At the same time, the Fusion method shows the lowest deviations, ranging from 1.9 mm to 2.9 mm, highlighting its effectiveness in refining data from both methods. The results achieved in this study match the findings of [4,10]. It was noticed that the fusion approach obtained more intensive data than individual RS techniques and thus resulted in more precise deformation detection than the standalone techniques. This is because the TLS data is lacking in the upper parts of the tank and delivers noise data. In contrast, the photogrammetric data obtains gaps in certain areas of the outer walls of the tank that could not be reduced without data integration. The fusion approach has successfully eliminated data outliers and noise in individual datasets by taking advantage of the complementary strengths of both techniques. The integration mitigates individual errors, enhances data completeness, and reduces noise, resulting in more accurate and reliable oil tank body deformation measurements.

The ability of the Fusion method to reduce mean deviations suggests that it effectively combines the strengths of TLS and UAV-SfM. Radius Difference Analysis shows that sections 1 and 10 have the highest radius differences, particularly in TLS and UAV-SfM. The Fusion method significantly reduces these values, suggesting that Fusion is particularly beneficial in sections with larger or more complex geometries. This could imply that Fusion's effectiveness is more pronounced in challenging measurement conditions. On the other hand, the circle center differences are generally more seen in UAV-SfM data, with values ranging from 3.0 mm to 4.0 mm. TLS shows more consistency and lower differences in the 2.4–4.0 mm range. The Fusion method consistently reduces these differences, with values between 2.2 mm and 3.8 mm, indicating better positional accuracy. Its ability to minimize circle center differences, particularly in complex sections like sections 8–10, underscores its value in applications where precise positional data is critical. This improvement could be vital in ensuring alignment and structural integrity in industrial processes, such as installing and maintaining cylindrical tanks.

Table 2: Differences of circular horizontal cross-sections for TLS, SfM, and Fusion datasets

Section	Average deviation (mm)			Radius difference (mm)			Circle centers difference (mm)		
	TLS	UAV - SfM	Fusion	TLS	UAV - SfM	Fusion	TLS	UAV - SfM	Fusion
1	4.2	5.5	2.9	4.1	6.6	2.4	2.6	3.1	2.2
2	3.6	5.0	2.2	3.6	6.1	2.3	2.5	3.0	2.2
3	3.7	4.9	2.4	3.7	5.5	1.4	2.5	3.0	2.3
4	3.2	4.7	1.9	2.5	5.3	1.1	2.4	2.9	2.2
5	3.6	4.8	2.3	2.3	4.6	1.3	2.5	3.0	2.3
6	3.4	4.6	2.1	2.4	4.2	1.7	2.8	3.2	2.5
7	3.1	4.4	2.0	2.0	3.9	1.6	2.8	3.1	2.5
8	3.6	4.7	2.3	2.3	4.7	1.8	3.4	3.6	2.9
9	4.2	5.0	2.8	3.5	5.1	1.9	3.6	3.8	3.0
10	4.9	5.0	2.9	5.8	5.4	2.3	4.0	4.0	3.8

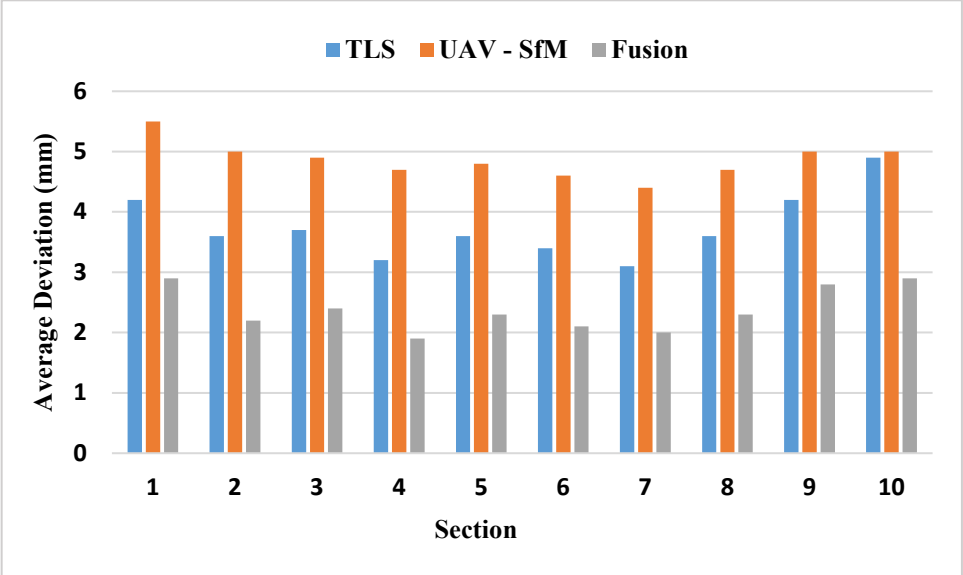

Figure 12: Average deviation (mm); (a) TLS (b) UAV-SfM (c) Fusion

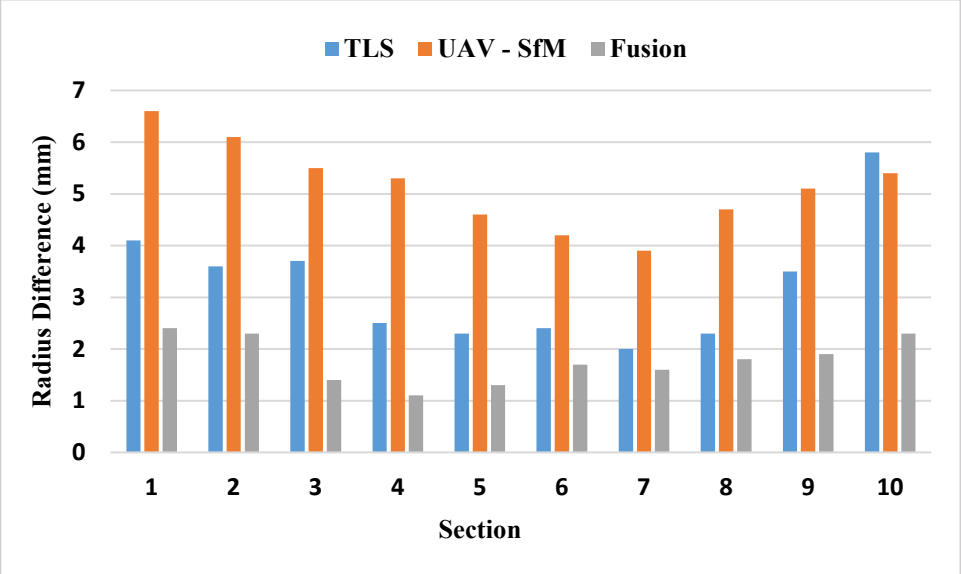

Figure 13: Radius difference; (a) TLS (b) UAV - SfM (c) Fusion

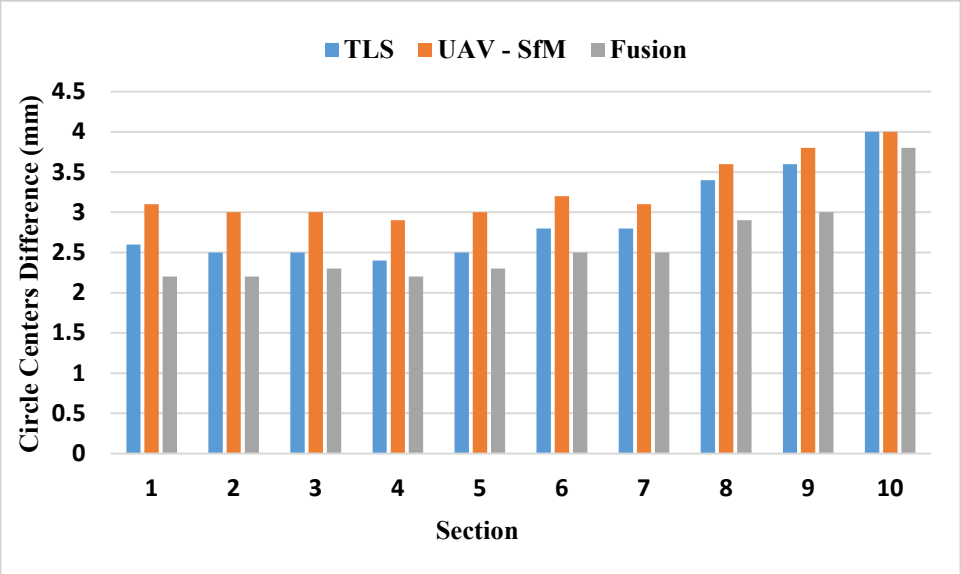

Figure 14: Circle centers difference; (a) TLS (b) UAV - SfM (c) Fusion

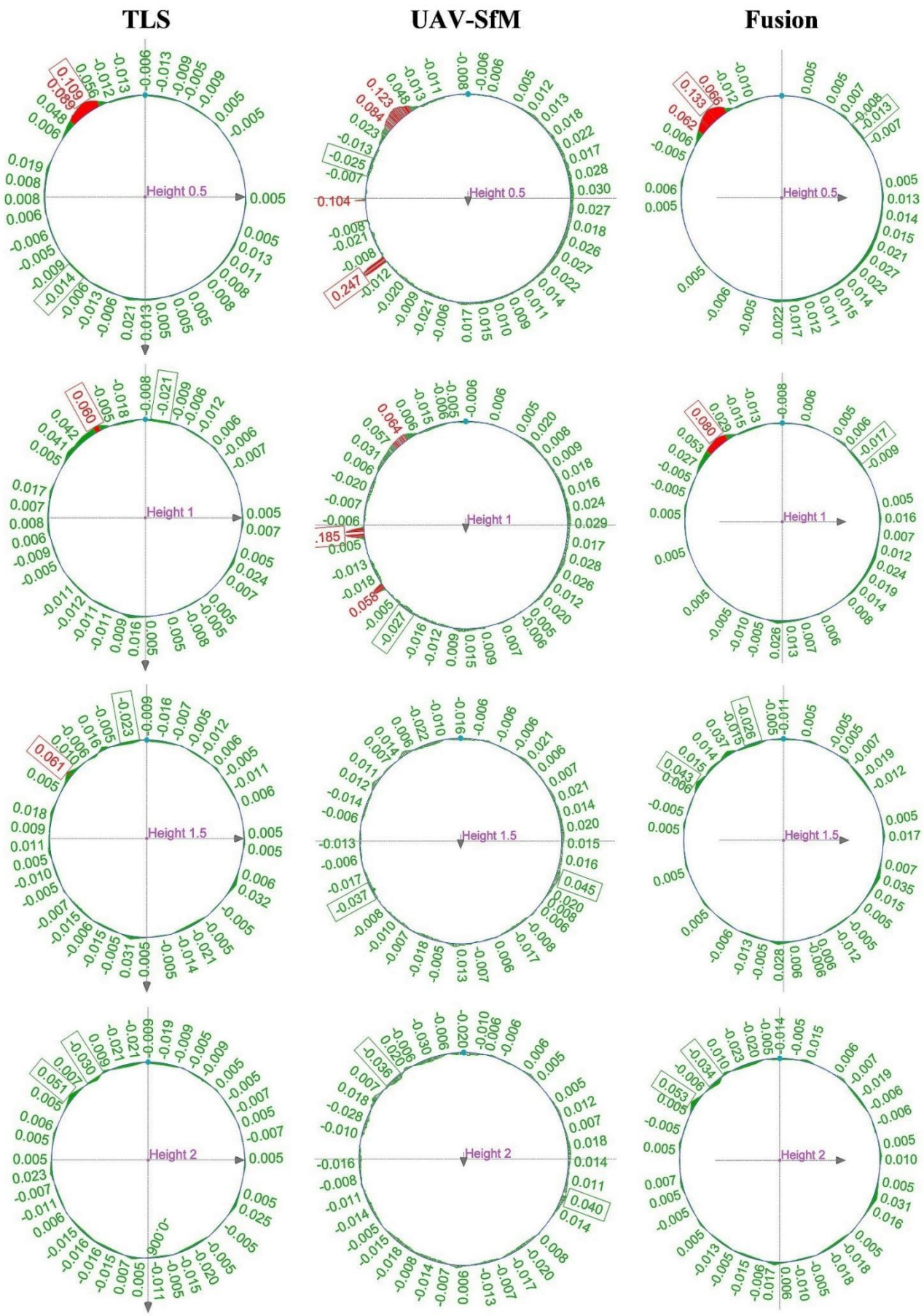

Figure 15: Circular Horizontal Cross-Section of the tank, (a) TLS, (b) UAV-SfM, (c) Fusion

An extra check of the integration process was performed for two vertical cross-sections Figure 16. This check examined the integration process. A reference approach was utilized, which consisted of fitting regression straight lines to the data obtained from the terrestrial laser scanning. Following that, the deviations for terrestrial scanning, UAV scanning, and the integrated model were calculated in relation to these straight lines Figure 16. In addition, the average deviations from the straight lines were calculated and presented in Table 3. The deviations were consistent and comparable to those of horizontal sections. The Fusion method reduces the average deviations for the TLS and UAV approaches, which are 8.5 mm and 9.4 mm, respectively, to 8 mm in sections 1 this is similar to Section 2.

Table 3: Average deviations from the straight lines on vertical cross-sections for TLS, SfM, and Fusion point clouds

Section	Average deviation (mm)		
	TLS	UAV - SfM	Fusion
0° - 180°	8.5	9.4	8.0
90° - 270°	9.1	9.8	8.4

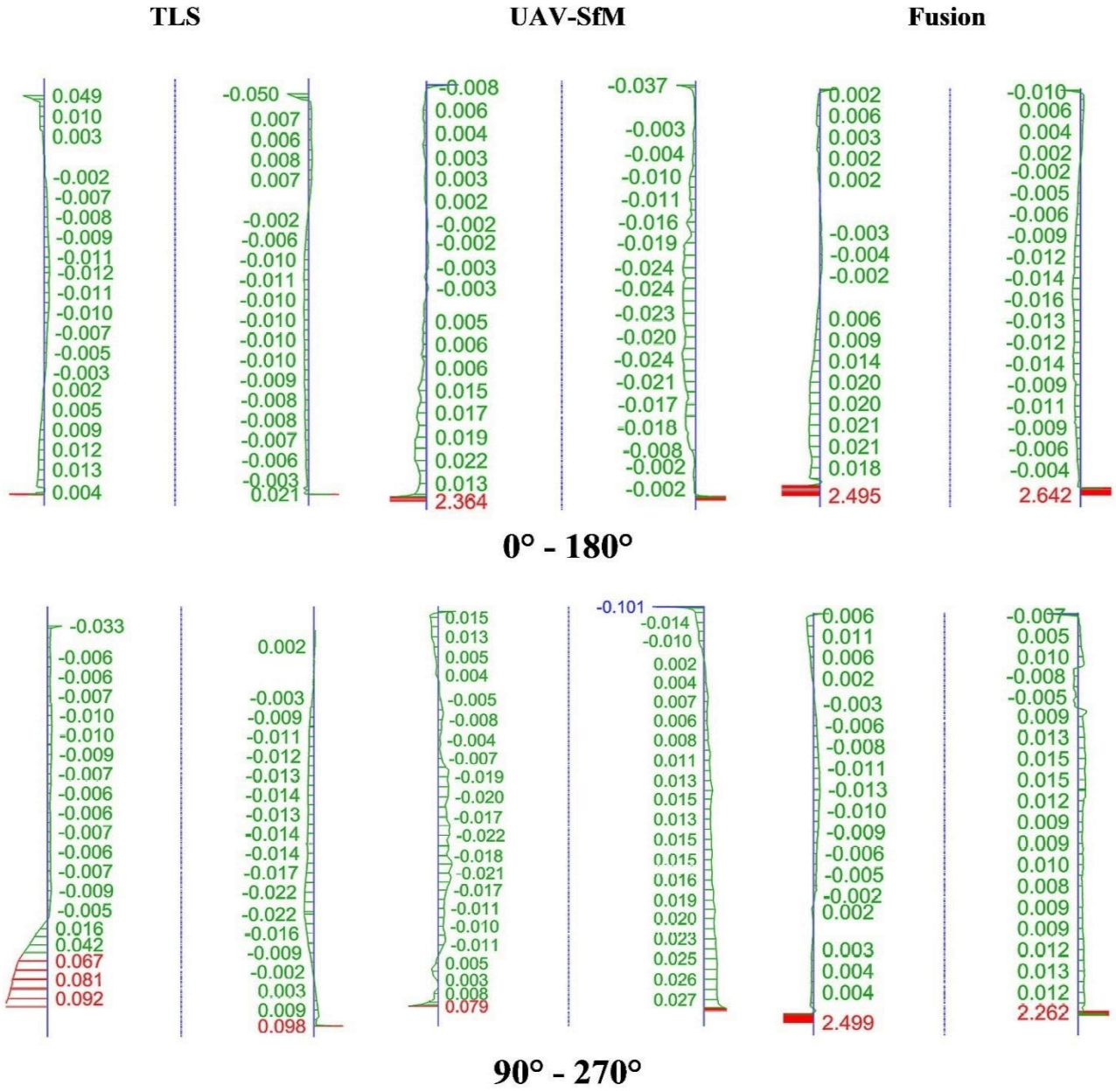

Figure 16: Vertical Cross-Section of the tank, (a) TLS, (b) UAV-SfM, (c) Fusion

4. Conclusion

The current paper presents a hybrid approach of RS data integration as the optimal solution to generate a virtual 3D model of industrial components and detect geometric deformation. This hybrid method uses a data fusion approach that integrates the resultant dense point clouds generated from two surveying techniques: TLS scans and UAV digital photogrammetry. The procedure is based on extracting synthetic 2D images from 3D laser data to combine with 2D photogrammetric images in a standalone co-registration approach based on SfM and MVS algorithms. In fact, after assessing their convergences and divergences, the hybrid approach was proposed to overcome the weakness of the proposed reconstruction methods. A part of the oil plant facility was selected as a case study. Both generated point clouds showed several limitations. For instance, relevant information, mainly related to the tank's roof, was missed in the TLS dataset, preventing the reproduction of the whole study area. Similarly, the small number of points composing the dense clouds generated from the UAV approach makes the model less reliable than that extracted by processing TLS data. Once the models' accuracy and comparability were assessed, data fusion methodology appeared as an effective solution to reconstruct physical industrial components precisely. The Fusion method's ability to reduce average deviations suggests that it effectively combines the strengths of TLS and UAV-SfM photogrammetry in one hybrid approach to detect tank surface deformation. This indicates its potential for high-precision applications, such as detailed structural analysis or maintenance in industrial environments. The Fusion method's consistent reduction of radius discrepancies and differences in circle centers across all sections suggests it enhances the reliability of cylindrical feature measurements and effectively compensates for positional inaccuracies in the photogrammetry standalone approach. The integration mitigates individual errors, enhances data completeness, and reduces noise, resulting in more accurate and reliable deformation measurements of the oil tank body surface. This study seeks to contribute to the growth of 3D modeling and deformation detection studies in the industrial sector by analyzing the benefits and limitations of this fusion methodology. The findings of this study will offer insights that can improve the efficiency, accuracy, and safety of facility management. Similar studies should be applied to different sites with various industrial objects, and multiple quality factors should be considered to verify further the methodology presented in this study.

Author contributions

Conceptualization, A. Al-Saedi, I. Alwan, and F. Abed.; data curation, A. Al-Saedi; formal analysis, A. Al-Saedi. and F. Abed; investigation, A. Al-Saedi, F. Abed, and I. Alwan.; methodology, A. Al-Saedi and F. Abed.; project administration, A. Al-Saedi. and F. Abed; resources, A. Al-Saedi; supervision, F. Abed and I. Alwan.; validation, A. Al-Saedi and F. Abed.; visualization, A. Al-Saedi.; writing—original draft preparation, A. Al-Saedi.; writing—review and editing, F. Abed and I. Alwan. All authors have read and agreed to the published version of the manuscript.

Funding

This research received no specific grant from any funding agency in the public, commercial, or not-for-profit sectors.

Data availability statement

The data that support the findings of this study are available on request from the corresponding author.

Conflicts of interest

The authors declare that there is no conflict of interest.

References

[1] I. Kadhim, F. M. Abed, J. M. Vilbig, V. Sagan, C. DeSilvey, Combining Remote Sensing Approaches for Detecting Marks of Archaeological and Demolished Constructions in Cahokia's Grand Plaza, Southwestern Illinois, Remote. Sens., 15 (2023) 1057. https://doi.org/10.3390/rs15041057

[2] L. Kovanič, M. Štroner, P. Blistan, R. Urban, R. Boczek, Combined ground-based and UAS SfM-MVS approach for determination of geometric parameters of the large-scale industrial facility – Case study, Measurement, 216 (2023) 112994. https://doi.org/10.1016/j.measurement.2023.112994

[3] A. S. Jaber, F. M. Abed, Revealing the potentials of 3D modelling techniques; a comparison study towards data fusion from hybrid sensors, IOP Conf. Ser.: Mater. Sci. Eng., 737, 2020, 012230. https://doi.org/10.1088/1757-899X/737/1/012230

[4] G. Lenda, U. Marmol, Integration of high-precision UAV laser scanning and terrestrial scanning measurements for determining the shape of a water tower, Measurement, 218 (2023) 113178. https://doi.org/10.1016/j.measurement.2023.113178

[5] L. Koranic, P. Blistan, R. Urban, M. Stronger, K. Pukanská , K. Bartoš , J. Palková, Analytical determination of geometric parameters of the rotary kiln by novel approach of tls point cloud segmentation, Appl. Sci., 10 (2020) 7652. https://doi.org/10.3390/app10217652

[6] Y. Alshawabkeh, A. Baik, Y. Miky, Integration of Laser Scanner and Photogrammetry for Heritage BIM Enhancement, ISPRS Int. J. Geo-Inf., 10 (2021) 316. https://doi.org/10.3390/ijgi10050316

[7] G. Kafataris, D. Skarlatos, M. Vlachos, Fusion of Direct Georeferenced Aerial Drone with Terrestrial Laser Scanner Data the Case of the Roman Baths of Amathus, Cyprus, ISPRS Annals of the Photogrammetry, Remote Sens. Spatial Inf. Sci., X-1/W1-2023 (2023)1057–1064. https://doi.org/10.5194/isprs-annals-X-1-W1-2023-1057-2023

[8] A. Capolupo, A. Maltese, M. Saponaro, D. Costantino, Integration of terrestrial laser scanning and UAV-SFM technique to generate a detailed 3D textured model of a heritage building, 11534 (2020). https://doi.org/10.1117/12.2574034

[9] L. Kovanič, P. Peťovský, B. Topitzer, P. Blišťan, Spatial Analysis of Point Clouds Obtained by SfM Photogrammetry and the TLS Method—Study in Quarry Environment, Land, 13 (2024) 614. https://doi.org/10.3390/land13050614

[10] J. Siwiec, G. Lenda, Integration of terrestrial laser scanning and structure from motion for the assessment of industrial chimney geometry, Measurement, 199 (2022) 111404. https://doi.org/10.1016/j.measurement.2022.111404

[11] J. Li, Y. Peng, Z. Tang, Z. Li, Three-Dimensional Reconstruction of Railway Bridges Based on Unmanned Aerial Vehicle–Terrestrial Laser Scanner Point Cloud Fusion, Buildings, 13 (2023) 2841. https://doi.org/10.3390/buildings13112841

[12] P. Budzianowski, P. Tysiac, Combined close range photogrammetry and terrestrial laser scanning for ship hull modelling, Geosciences, 9 (2019) 242. https://doi.org/10.3390/geosciences9050242

[13] M. Guo, X. Tang, Y. Zhao, Y. Liu, Z. Chen, L. Zhu, K. Guo, Monitoring Scheme of Liquified Natural Gas External Tank Using Air–Space–Land Integration Multisource Remote Sensing, Sens. Mater., 36 (2024) 373–392. https://doi.org/10.18494/SAM4603

[14] A. Soni, S. Robson, B. Gleeson, Structural monitoring for the rail industry using conventional survey, laser scanning and photogrammetry, Appl. Geomat., 7 (2015) 123–138. https://doi.org/10.1007/s12518-015-0156-1

[15] A. Z. Khalaf, A. S. J. Al-Saedi, Assessment of Structure with Analytical Digital Close Range Photogrammetry, Eng. Technol. J., 34 (2016) 2140–2151. http://dx.doi.org/10.30684/etj.34.11A.18

[16] "Leica TS09 Plus." [Online]. Available: https://www.sccssurvey.co.uk/leica-flexline-ts09plus-total-station.html

[17] "CHCNAV i50 GNSS." [Online]. Available: https://chcnav.com/uploads/i50_DS_EN.pdf

[18] Leica ScanStation C40." [Online]. Available: https://leica-geosystems.com/products/laser-scanners/scanners/leica-scanstation-p40--p30

[19] "DJI Phantom 4 Pro." [Online]. Available: https://www.dji.com/sk/phantom-4-pro

[20] R. M. Ridha, I. A. Alwan, H. S. Ismael, Accuracy assessment of UAV automated 3D city model for urban planning, AIP Conf. Proc., 2793, 2023. https://doi.org/10.1063/5.0162664

[21] R. M. Ridha, I. A. Alwan, H. S. Ismael, Accuracy assessment of 3D model reconstructed from UAV images by the distribution of the ground control points (GCPs), AIP Conf. Proc., 3105, 2024. https://doi.org/10.1063/5.0212203

[22] A. M. Noori, A. S. J. Al-Saedi, F. M. Abed, Optimizing Application of UAV-Based SfM Photogrammetric 3D Mapping in Urban Areas, J. Sci., 65 (2024) 2958–2975. https://doi.org/10.24996/ijs.2024.65.5.46

[23] A. Z. Khalaf, N. S. Mohammed, F. S. A. Al-hasoon, Accuracy Assessment of Analytical Orientation Process in Close range Photogrammetry, Eng. Technol. J., 34 (2016) 2739–2753. https://doi.org/10.30684/etj.34.14A.17

[24] A. H. Hadi, A. Z. Khalaf, Accuracy Assessment of Establishing 3D Real Scale Model in Close-Range Photogrammetry with Digital Camera, Eng. Technol. J., 40 (2022) 1492-1509. http://dx.doi.org/10.30684/etj.2022.132233.1097

[25] Leica Cyclone." [Online]. Available: https://leica-geosystems.com/products/laser-scanners/software/leica-cyclone

[26] W. Moussa, K. Wenzel, M. Rothermel, M. Abdel-Wahab, D. Fritsch, Complementing TLS Point Clouds by Dense Image Matching, Int. J. Heritage in the Digital Era, 2 (2013) 453-470. http://dx.doi.org/10.1260/2047-4970.2.3.453

[27] Agisoft Metashape", [Online]. Available: https://www.agisoft.com/features/professional-edition/

[28] Reality Capture." [Online]. Available: https://www.capturingreality.com/

[29] CloudCompare." [Online]. Available: https://www.danielgm.net/cc/

[30] A. S. J. Al-Saedi, F. M. Abed, I. A. Alwan, Geometric Quality Analysis of Terrestrial Laser Scanning Data for Industrial Usage, IIUM Eng. J., 25 (2024) 148–166. http://dx.doi.org/10.31436/iiumej.v25i2.3211

[31] Leica Cyclone." [Online]. Available: https://leica-geosystems.com/products/laser-scanners/software/leica-cyclone/ leica-cyclone-3dr